Relativistic energy loss and induced photon emission in the interaction of a dielectric sphere with an external electron beam

F. J. García de Abajo
Departamento de CCIA, Facultad de Informática, and Departamento de Física de Materiales, Facultad de Química, UPV/EHU, San Sebastián, Spain
(Received 26 May 1998)

An analytical expression for the energy loss suffered by a fast electron passing near a homogeneous dielectric sphere is derived within a fully relativistic approach. The sphere is described by a frequency-dependent dielectric function. The electromagnetic field induced by the passage of the electron is then obtained by expressing the solution of Maxwell's equations for this geometry in terms of the scattering of the multipole expansion of the incoming electromagnetic field at the sphere. The energy loss is derived from the induced field acting back on the electron. The variation of the energy-loss spectra with both the radius of the sphere and the impact parameter of the electron trajectory is studied in detail. Part of the energy loss is transformed into radiation, which is also investigated. For spheres characterized by real dielectric functions, like those of ionic materials in the transparency-frequency region, it is shown that the entire energy loss is transformed into radiation. Examples of loss spectra and radiation emission spectra are given for a material described by a Drude-like dielectric function (e.g., Al) and for SiO_2. [S0163-1829(99)12103-9]

I. INTRODUCTION

Scanning transmission electron microscopy (STEM) has proved to be a powerful technique for determining local chemical and electronic structure, particularly when using the excitation of target atoms.[1] The relatively more intense low-energy, valence excitation part of the spectrum is also of considerable interest,[2–5] though its theoretical analysis is not so direct. Under typical STEM conditions, a fast 100-keV electron beam is focused on an area with diameter as small as 0.2 nm with a controlled position on the sample. This permits electron-energy-loss spectroscopy (EELS) with high-lateral resolution to be performed. The position of the features in the low-energy loss spectra are directly related to the geometry of the specimen under study, and hence, its analysis may provide valuable information on this aspect as well as yielding local chemical or electronic data.

Nonrelativistic, analytical descriptions of EELS have been limited to simple geometries such as planes,[6,7] cylinders,[8] hyperbolic wedges,[9] isolated spheres,[10–12] two coupled spheres,[13] spheroids,[14] or the combination of a spherical interface and a plane.[15,16] More recently, the boundary-charge method has allowed calculations in more complex geometries[17–19] by self-consistently solving the induced charge-density distribution.

The large velocity of STEM electrons ($v>0.5c$) implies the need for relativistic corrections. Furthermore, when the sample under study, of characteristic dimension a, has modes of frequency ω such that the wavelength of the radiation for that frequency $\lambda=c/\omega$ is smaller than a (i.e., $\omega a/c>1$), the effects of retardation emerge as frequency shift and splitting of highly delocalized, low-order modes. The latter can be efficiently excited by fast electrons, for which the effective-impact parameter range of interaction with the target is v/ω.

The relativistic analytical treatments of EELS have been even more strongly limited to the cases of planar surfaces[20,21] and cylinders.[8] Numerical methods have also been employed to explore more complex geometries by making use of the transfer-matrix approach for periodic systems[22,23] or by generalizing the nonrelativistic boundary-charge method by adding boundary-current distributions to be solved self-consistently.[24] Studies of energy losses from small spheres by the boundary-charge method revealed that radiation corrections could still be appreciable even in the absence of Cherenkov effects [i.e., for $(v/c)^2\mathrm{Re}\{\epsilon\}<1$] or retardation corrections ($\omega a/c<1$). Therefore, further analytical studies would be useful in order to gain in substantial understanding of the relativistic effects involving electron energy-loss phenomena.

Fuchs and Kliewer[25] studied analytically the effects of retardation on the polariton modes of small LiF spheres finding out a rich structure of magnetic and electric modes, characterized by frequencies and radiative widths dependent upon the sphere radius. Here, their work is extended to other dielectric materials and to include the contribution of each mode to the energy-loss probability.

An analytical solution for the energy loss suffered by a fast electron passing near a homogeneous sphere is derived. The exact solution of Maxwell's equations for this geometry is expanded in terms of multipoles of the electromagnetic field, made up of both the bare field set up by the fast charge and the induced field, resulting from the scattering of the bare field at the sphere. The induced field acts back on the projectile producing a net retarding force responsible for the electron-energy loss.

As a simplifying assumption, the sphere will be described by a frequency-dependent dielectric function $\epsilon(\omega)$, in the spirit of the local response approximation, valid for the large velocities under consideration.[26] Furthermore, relativistic effects in the dielectric function[27] will be neglected, since we will be interested in low-energy valence losses.

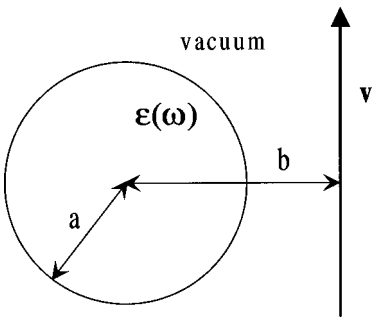

FIG. 1. Schematic representation of the geometry under study: an electron is moving in vacuum with constant velocity **v** and impact parameter *b* with respect to the center of a nonmagnetic homogeneous sphere of radius *a* described by a frequency-dependent dielectric function $\epsilon(\omega)$.

The formalism and details of the theory are presented in Sec. II. The application to spheres of different radius and trajectories with various impact parameters is discussed in Sec. III. Comparison with former nonrelativistic[10,11] results is also offered.

Part of the energy loss is transformed into induced radiation, via coupling with the radiative modes of the sphere. The analysis of this radiation is given in Sec. IV. In particular, it is found that the energy loss goes entirely into radiation when the dielectric function is real. This effect can be relevant in STEM studies of ionic compounds like LiF or SiO_2 characterized by large real dielectric functions in the transparency frequency region below 9 eV.

Finally, the main conclusions will be summarized in Sec. V. Atomic units (a.u., i.e., $e=m=\hbar=1$) will be used from now on, unless otherwise specified.

II. ANALYTICAL SOLUTION FOR THE ENERGY LOSS

Let us consider a fast electron moving along a straight-line trajectory with constant velocity v and passing near a homogeneous sphere located in vacuum, as shown in Fig. 1. The sphere will be assumed to be nonmagnetic and described by a frequency-dependent dielectric function $\epsilon(\omega)$. The energy loss suffered by the electron will be obtained from the retarding force that the induced electromagnetic field produces when it acts back on the electron.

Without any loss of generality, the electron trajectory will be chosen parallel to the *z* axis with impact parameter *b* with respect to the origin of coordinates, made to coincide with the center of the sphere of radius *a*, as shown in Fig. 1.

The electromagnetic field satisfies the Maxwell equations, which can be solved for spherically symmetric objects like our sphere by using a multipole expansion.

A. Scalar functions

The multipole expansion of the electromagnetic field can be conveniently performed in frequency space ω using the dyadic identity, valid for any smooth vector field and in particular for the electric field **E**,[28]

$$\mathbf{E}=\nabla\frac{1}{\nabla^2}(\nabla\cdot\mathbf{E})+\mathbf{L}\frac{1}{L^2}(\mathbf{L}\cdot\mathbf{E})-(\nabla\times\mathbf{L})\frac{1}{L^2\nabla^2}[(\mathbf{L}\times\nabla)\cdot\mathbf{E}],$$

where $\mathbf{L}=-i\mathbf{r}\times\nabla$ is the orbital angular-momentum operator. This expression permits longitudinal, magnetic, and electric scalar functions to be defined as[28]

$$\psi^L=\frac{1}{\nabla^2}\nabla\cdot\mathbf{E},$$

$$\psi^M=\frac{1}{L^2}\mathbf{L}\cdot\mathbf{E}, \tag{1}$$

and

$$\psi^E=\frac{-ik}{L^2\nabla^2}(\mathbf{L}\times\nabla)\cdot\mathbf{E}, \tag{2}$$

respectively, so that the electric field reduces to

$$\mathbf{E}=\nabla\psi^L+\mathbf{L}\psi^M-\frac{i}{k}\nabla\times\mathbf{L}\psi^E, \tag{3}$$

where $k=\omega/c$. In a vacuum free of charges and currents, these scalar functions satisfy the wave equation

$$(\nabla^2+k^2)\psi=0. \tag{4}$$

Now, using the Maxwell equation $\nabla\times\mathbf{E}=ik\mathbf{H}$ and Eq. (4), one finds the magnetic field[28]

$$\mathbf{H}=-\frac{i}{k}\nabla\times\mathbf{L}\psi^M-\mathbf{L}\psi^E. \tag{5}$$

Since we are interested in the electromagnetic field in the vacuum where the electron is moving, the contribution of the longitudinal scalar function ψ^L, which describes an instant propagation of the fields [i.e., it plays in Eq. (3) the same role as the electric-scalar potential in the nonrelativistic limit], must cancel the contribution of the pole of $1/\nabla^2$ in Eq. (2), also leading to instant propagation.[28] Hence, we can set $\psi^L=0$ in Eq. (3) and take $\nabla^2=-k^2$ in Eq. (2) [see Eq. (4)], that is, we redefine

$$\psi^E=\frac{i}{k}\frac{1}{L^2}(\mathbf{L}\times\nabla)\cdot\mathbf{E}. \tag{6}$$

Therefore, the longitudinal modes are explicitly left out of the final result for the case of external trajectories.

The multipole expansion of the bare electromagnetic field (i.e., in the absence of the sphere) set up by the electron in the noted vacuum region has to be made up of spherical waves with no net flux, since an electron freely moving in vacuum cannot give rise to any radiation. Therefore, the scalar functions that describe this external field have to have the form

$$\psi^{M,\mathrm{ext}}(\mathbf{r})=\sum_{l=1}^{\infty}\sum_{m=-l}^{l}i^l j_l(kr)Y_{lm}(\Omega_{\mathbf{r}})\psi_{lm}^{M,\mathrm{ext}}, \tag{7}$$

and

$$\psi^{E,\mathrm{ext}}(\mathbf{r})=\sum_{l=1}^{\infty}\sum_{m=-l}^{l}i^l j_l(kr)Y_{lm}(\Omega_{\mathbf{r}})\psi_{lm}^{E,\mathrm{ext}}, \tag{8}$$

where $j_l(x)$ are spherical Bessel functions, $(r,\Omega_{\mathbf{r}})$ are the spherical coordinates of $\mathbf{r}$, and the sums run over spherical harmonics Y_{lm}. These expressions are valid for the region $a<r<b$, that is, in the spherical shell of vacuum outside the sphere of radius a that does not overlap the electron trajectory of impact parameter b (see Fig. 1).

B. Multipoles for a fast electron

The scalar functions $\psi^{M,\mathrm{ext}}(\mathbf{r})$ and $\psi^{E,\mathrm{ext}}(\mathbf{r})$ can be obtained from the bare electric field produced by the electron (its -1 charge is taken into account),[29]

$$\mathbf{E}^{\mathrm{ext}}(\mathbf{r})=\left(\nabla-\frac{ik\mathbf{v}}{c}\right)\int dt e^{\mathbf{i}\omega t}G_0(\mathbf{r}-\mathbf{r}_t),$$

where

$$G_0(\mathbf{r}-\mathbf{r}_t)=\frac{e^{\mathbf{i}k|\mathbf{r}-\mathbf{r}_t|}}{|\mathbf{r}-\mathbf{r}_t|} \tag{9}$$

is the Green function of Eq. (4), $\mathbf{r}_t=\mathbf{r}_0+\mathbf{v}t$ describes the electron trajectory, $\mathbf{v}=(0,0,v)$ is the velocity vector, and the cylindrical coordinates of $\mathbf{r}_0$ are denoted (b,φ_0,z_0).

Here, it is convenient to expand the Green function in terms of multipoles,[30]

$$G_0(\mathbf{r},\mathbf{r}_t)=4\pi k\sum_{l=0}^{\infty}\sum_{m=-l}^{l}j_l(kr)h_l^{(+)}(kr_t)Y_{lm}(\Omega_{\mathbf{r}})Y_{lm}^*(\Omega_{\mathbf{r}_t}), \tag{10}$$

where $h_l^{(+)}(x)=\mathbf{i}h_l^{(1)}(x)$ is the spherical Hankel function (the notation of Messiah[31] has been adopted). This expression is valid for $r<r_t$, which is the case for external trajectories and $\mathbf{r}$ near the sphere surface. Then, the electric field becomes

$$\mathbf{E}^{\mathrm{ext}}(\mathbf{r})=\left(\nabla-\frac{ik\mathbf{v}}{c}\right)\sum_{l=0}^{\infty}\sum_{m=-l}^{l}j_l(kr)Y_{lm}(\Omega_{\mathbf{r}})\phi_{lm}, \tag{11}$$

where

$$\phi_{lm}=4\pi k\int dt e^{\mathbf{i}\omega t}h_l^{(+)}(kr_t)Y_{lm}^*(\Omega_{\mathbf{r}_t}).$$

The integral in this equation can be performed analytically as shown in Appendix A. Using the result given in Eqs. (A1), (A2), and (A8), one finds

$$\phi_{lm}=4\pi k\frac{A_{lm}^+}{\omega}K_m\left(\frac{\omega b}{v\gamma}\right)e^{-\mathbf{i}m\varphi_0-\mathbf{i}\omega z_0/v}, \tag{12}$$

where K_m is the modified Bessel function of order m and $\gamma=1/\sqrt{1-(v/c)^2}$ accounts for the Lorentz contraction of the impact parameter b. In the case under consideration, where the electron is moving in vacuum, the coefficient A_{lm}^+, defined by Eq. (A9), depends exclusively on v/c. An exponential dependence on b at large-impact parameters is introduced here via K_m functions.

Inserting Eq. (11) into Eq. (1), using the relation $\mathbf{L}\cdot\nabla=0$, and performing the substitutions $\mathbf{L}\cdot\mathbf{v}=L_z v\to mv$ and $L^2\to l(l+1)$, one finds that Eq. (7) is indeed correct, provided one defines expansion coefficients

$$\psi_{lm}^{M,\mathrm{ext}}=\frac{-4\pi i^{1-l}kv}{c^2}\frac{mA_{lm}^+}{l(l+1)}K_m\left(\frac{\omega b}{v\gamma}\right)e^{-\mathbf{i}m\varphi_0-\mathbf{i}\omega z_0/v}. \tag{13}$$

The component $l=0$ is left out, since it does not contribute to the fields.

Similarly, the electric-scalar function is given by Eq. (8) with coefficients

$$\psi_{lm}^{E,\mathrm{ext}}=\frac{-2\pi i^{1-l}k}{c\gamma}\frac{B_{lm}}{l(l+1)}K_m\left(\frac{\omega b}{v\gamma}\right)e^{-\mathbf{i}m\varphi_0-\mathbf{i}\omega z_0/v}, \tag{14}$$

where

$$B_{lm}=A_{l,m+1}^+\sqrt{(l+m+1)(l-m)}-A_{l,m-1}^+\sqrt{(l-m+1)(l+m)}. \tag{15}$$

The derivation of Eq. (14) requires a more detailed analysis, which is summarized in Appendix B.

C. Scattering by a sphere

For an arbitrary, spherically symmetric medium, the matching conditions satisfied by the fields (i.e., the continuity of the normal displacement, the parallel electric field, and the magnetic field) reduce, after using Eqs. (3) and (5), to the continuity of ψ^M, $\epsilon\psi^E$, $\partial\psi^M/\partial r$, and $(1+r\partial/\partial r)\psi^E$.[28] Thus, magnetic and electric scalar functions are decoupled in a spherically symmetric system.

The total electromagnetic fields are the superposition of the external fields and the induced or scattered fields, that is, $\mathbf{E}=\mathbf{E}^{\mathrm{ext}}+\mathbf{E}^{\mathrm{ind}}$ and $\mathbf{H}=\mathbf{H}^{\mathrm{ext}}+\mathbf{H}^{\mathrm{ind}}$. In general, the electromagnetic field in vacuum is a combination of outgoing and incoming waves, represented by spherical Hankel functions $h_l^{(+)}(kr)$ and $h_l^{(-)}(kr)$, respectively. In our case, the induced fields find their sources in the charges and currents induced by the external electron in the sphere. Therefore, for $\mathbf{r}$ outside the sphere, the induced fields have to be a combination of only outgoing waves, that is,

$$\psi^{M,\mathrm{ind}}(\mathbf{r})=\sum_{l=1}^{\infty}\sum_{m=-l}^{l}i^l h_l^{(+)}(kr)Y_{lm}(\Omega_{\mathbf{r}})\psi_{lm}^{M,\mathrm{ind}} \tag{16}$$

and

$$\psi^{E,\mathrm{ind}}(\mathbf{r})=\sum_{l=1}^{\infty}\sum_{m=-l}^{l}i^l h_l^{(+)}(kr)Y_{lm}(\Omega_{\mathbf{r}})\psi_{lm}^{E,\mathrm{ind}}. \tag{17}$$

Actually, applying the boundary conditions stated above, one finds that these equations are correct and that the relation between the components of external and induced scalar functions is given by the scattering matrix[32] in the same way as in the partial-wave analysis of the Schrödinger equation for a finite-range spherical potential. More precisely,

$$\psi_{lm}^{M,\mathrm{ind}}=t_l^M\psi_{lm}^{M,\mathrm{ext}} \tag{18}$$

and

$$\psi_{lm}^{E,\mathrm{ind}}=t_l^E\psi_{lm}^{E,\mathrm{ext}}, \tag{19}$$

where the scattering-matrix elements t_l^M and t_l^E are independent of m due to the spherical symmetry.

Outside the sphere, the scalar functions satisfy Eq. (4), whereas in the inside region they satisfy the equation $(\nabla^2 + k^2\epsilon)\psi = 0$. Now, solving these two equations with the matching conditions stated above, there is only one solution (except for a normalization constant and y_{lm} angular dependence) for each l that behaves like

$$\psi \sim j_l(kr) + t_l h_l^{(+)}(kr), \quad r > a,$$

where the first term is the zero-flux solution for an infinite vacuum [i.e., the terms of the externally applied field given by Eqs. (7) and (8)] and the second term is the scattered part (induced outgoing field). This equation defines the values of the scattering matrix, commonly written in terms of phase shifts δ_l as $t_l = \sin\delta_l \exp(i\delta_l)$.

Equations (18) and (19) are general for spherically symmetric targets. For homogeneous spheres one recovers expressions familiar from Mie's scattering theory.[33] More precisely,

$$t_l^M = \frac{-j_l(\rho_0)\rho_1 j_l'(\rho_1) + \rho_0 j_l'(\rho_0) j_l(\rho_1)}{h_l^{(+)}(\rho_0)\rho_1 j_l'(\rho_1) - \rho_0 [h_l^{(+)}(\rho_0)]' j_l(\rho_1)}, \quad (20)$$

and

$$t_l^E = \frac{-j_l(\rho_0)[\rho_1 j_l(\rho_1)]' + \epsilon[\rho_0 j_l(\rho_0)]' j_l(\rho_1)}{h_l^{(+)}(\rho_0)[\rho_1 j_l(\rho_1)]' - \epsilon[\rho_0 h_l^{(+)}(\rho_0)]' j_l(\rho_1)}, \quad (21)$$

where $\rho_0 = ka$, $\rho_1 = ka\sqrt{\epsilon}$ with $\mathrm{Im}\{\rho_1\} > 0$, and the prime elsewhere denotes differentiation with respect to ρ_0 and ρ_1.

The modes of a homogeneous sphere are given by the zeros of the denominators of Eqs. (20) and (21), in agreement with the result found by Fuchs and Kliewer,[25] who studied polariton modes of LiF spheres. Here, we will focus on higher-energy modes as shown in Fig. 2 for spheres described by the Drude dielectric function

$$\epsilon(\omega) = 1 - \frac{\omega_p^2}{\omega(\omega + i\eta)}. \quad (22)$$

(The case of aluminum corresponds to bulk-plasma energy $\omega_p = 15$ eV and electron gas damping $\eta = 1.06$ eV.) The loss probability must be governed by the imaginary part of the scattering-matrix elements so that these quantities have been represented in Fig. 2 as a function of frequency ω. Even for zero damping [Figs. 2(a) and 2(b)], the natural oscillations have a finite width, clearly seen in the case of the electric modes (solid curves). When a finite damping is added [solid curves in Figs. 2(c)–2(f)], the increase in the widths is given by $\approx \eta$. Both the shift of the eigenfrequencies towards lower values and the increase in the widths with increasing sphere radius are in qualitative agreement with the case of LiF polaritons.[25]

Expanding the denominator of Eq. (21) in the small sphere limit for real dielectric functions, the real part of the electric eigenfrequencies ω_r are found to satisfy

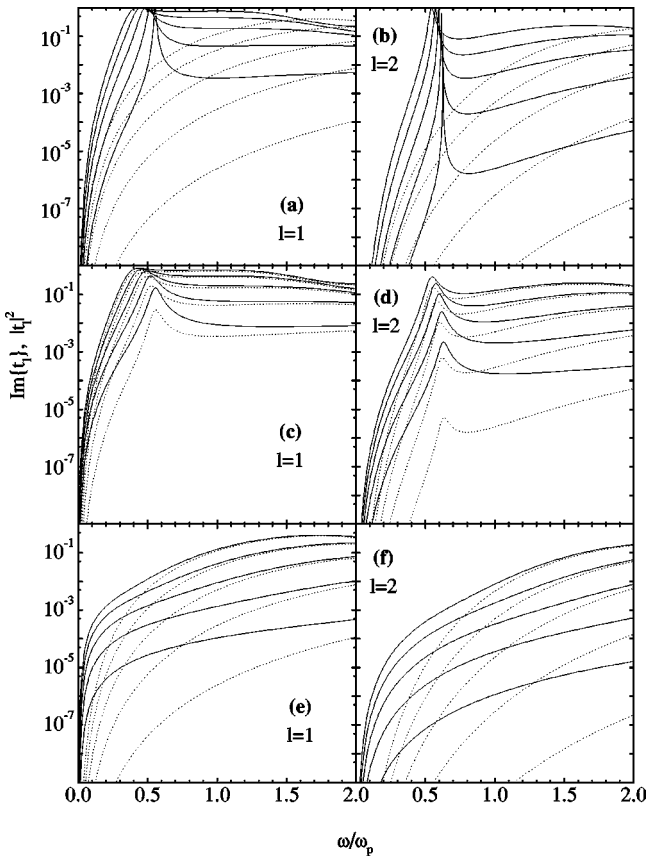

FIG. 2. (a) Imaginary part of the scattering-matrix elements $\mathrm{Im}\{t_l^M\}$ (broken curves) and $\mathrm{Im}\{t_l^E\}$ (solid curves), given by Eqs. (20) and (21), respectively, for $l=1$. The sphere is described by a Drude dielectric function with damping $\eta = 0$. (b) The same as (a) for $l=2$. (c) $\mathrm{Im}\{t_l^E\}$ (solid curves) and $|t_l^E|^2$ (broken curves) for $\eta = 0.07\omega_p$ and $l=1$. (d) The same as (c) for $l=2$. (e) $\mathrm{Im}\{t_l^M\}$ (solid curves) and $|t_l^M|^2$ (broken curves) for $\eta = 0.07\omega_p$ and $l=1$. (f) The same as (e) for $l=2$. The curves in each plot correspond to different sphere radius: $\omega_p a/c = 0.2,\ 0.6,\ 1,\ 1.4$, and 1.8 (the larger the radius, the higher the scattering-matrix element).

$$\epsilon l + l + 1 + \frac{1}{2}\left(\frac{\omega_r a}{c}\right)^2 \times \left[\frac{l+1}{2l-1} - \epsilon\frac{3(2l+1)}{(2l+3)(2l-1)} - \epsilon^2\frac{l}{2l+3}\right] \approx 0.$$

Now, for the dielectric function of Eq. (22) in the $\eta \to 0$ limit, one finds the real part of the dipole eigenfrequency $(l=1)$

$$\omega_r/\omega_p \approx \sqrt{\frac{1+0.1\alpha^2}{3+1.1\alpha^2}}, \quad (23)$$

where $\alpha = \omega_p a/c$. Similarly, the imaginary part is given by

$$\omega_i \approx \frac{-\alpha^3}{9+3.3\alpha^2}\frac{\omega_r^2}{\omega_p}. \quad (24)$$

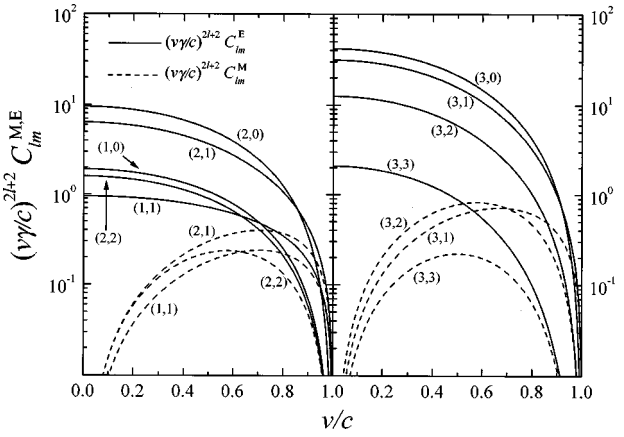

FIG. 3. Dependence of the coupling constants C_{lm}^{M} [broken curves; Eq. (30)] and C_{lm}^{E} [solid curves; Eq. (31)] on electron velocity for different values of (l,m) with $l=1,2$ (left part) and $l=3$ (right part), as shown in the insets. Notice that $C_{lm}^{M}=C_{l,-m}^{M}$, $C_{lm}^{E}=C_{l,-m}^{E}$, and $C_{l0}^{M}=0$.

D. Energy loss

The positive energy loss suffered by the fast electron passing near the sphere can be related to the force exerted by the induced electric field $\mathbf{E}^{\rm ind}$ acting on it as

$$\Delta E^{\rm loss}=\int dt\,\mathbf{v}\cdot\mathbf{E}^{\rm ind}(\mathbf{r}_t,t)=\int_0^\infty \omega d\omega\,\Gamma^{\rm loss}(\omega), \quad (25)$$

where

$$\Gamma^{\rm loss}(\omega)=\frac{1}{\pi\omega}\int dt\,{\rm Re}\{e^{-i\omega t}\mathbf{v}\cdot\mathbf{E}^{\rm ind}(\mathbf{r}_t,\omega)\} \quad (26)$$

is the so-called loss probability.

Equation (26) can be divided into the contributions of magnetic and electric modes,

$$\Gamma^{\rm loss}=\Gamma^{M,{\rm loss}}+\Gamma^{E,{\rm loss}},$$

coming from the magnetic and electric parts of the induced electric field $\mathbf{L}\psi^{M}$ and $(-i/k)\nabla\times\mathbf{L}\psi^{E}$, respectively. $\Gamma^{M,{\rm loss}}$ can be calculated by inserting Eq. (16) into Eq. (3) and this in turn into Eq. (26). Noticing that only the electric-field component along the direction of motion (the z axis here) contributes to produce energy loss, using the results of Appendix A, and making the substitution $\mathbf{v}\cdot\mathbf{L}=vL_z\to mv$, one obtains

$$\Gamma^{M,{\rm loss}}(\omega)=\sum_{l=1}^{\infty}\sum_{m=-l}^{l}\frac{mv}{\pi\omega^2}K_m\left(\frac{\omega b}{v\gamma}\right)\times{\rm Re}\{(A_{lm}^{+})^{*}e^{im\varphi_0+i\omega z_0/v}i^{-l}\psi_{lm}^{M,{\rm ind}}\}. \quad (27)$$

Similarly, $\Gamma^{E,{\rm loss}}$ can be calculated starting from Eq. (17) and using similar techniques to those followed in Appendix B to obtain Eq. (14), except that one has now $\mathbf{v}\cdot(\nabla\times\mathbf{L})=(-iv/2)(\partial_{-}L_{+}-\partial_{+}L_{-})$. One finds

$$\Gamma^{E,{\rm loss}}(\omega)=\sum_{l=1}^{\infty}\sum_{m=-l}^{l}\frac{c}{2\pi\omega^2\gamma}K_m\left(\frac{\omega b}{v\gamma}\right)\times{\rm Re}\{B_{lm}^{*}e^{im\varphi_0+i\omega z_0/v}i^{-l}\psi_{lm}^{E,{\rm ind}}\}. \quad (28)$$

Finally, inserting Eqs. (13) and (14) into Eqs. (18) and (19), and these in turn into Eqs. (27) and (28), one finds that the electron energy-loss probability per-unit-energy range ω for an electron passing outside a dielectric sphere with velocity v and impact parameter b relative to the center of the sphere (see Fig. 1) is given by

$$\Gamma^{\rm loss}(\omega)=\frac{1}{c\omega}\sum_{l=1}^{\infty}\sum_{m=-l}^{l}K_m^2\left(\frac{\omega b}{v\gamma}\right)\times[C_{lm}^{M}\,{\rm Im}\{t_l^{M}\}+C_{lm}^{E}\,{\rm Im}\{t_l^{E}\}], \quad (29)$$

where the positive coefficients

$$C_{lm}^{M}=\frac{1}{l(l+1)}\left|\frac{2mv}{c}A_{lm}^{+}\right|^2 \quad (30)$$

and

$$C_{lm}^{E}=\frac{1}{l(l+1)}\left|\frac{1}{\gamma}B_{lm}\right|^2 \quad (31)$$

depend exclusively on the ratio v/c. The first values of A_{lm}^{+} and B_{lm} [see Eqs. (A9) and (15)] are

$$A_{10}^{+}=\sqrt{\frac{3}{\pi}}\frac{i}{(v/c)^2},\quad B_{10}=-\sqrt{\frac{12}{\pi}}\frac{1}{(v/c)^2\gamma},$$

$$A_{11}^{+}=-A_{1,-1}^{+}=-\sqrt{\frac{3}{2\pi}}\frac{1}{(v/c)^2\gamma},$$

$$B_{11}=-B_{1,-1}=-\sqrt{\frac{6}{\pi}}\frac{i}{(v/c)^2}.$$

The dependence of $\Gamma^{\rm loss}(\omega)$ on both the sphere radius a and its dielectric function $\epsilon(\omega)$ shows up only via the velocity-independent scattering-matrix elements of the sphere for magnetic and electric components t_l^{M} and t_l^{E}, respectively (see Sec. II C). Since $l=0$ does not contribute to the loss, this term has been explicitly left out of the sum in Eq. (29).

Equation (29) has a form similar to its nonrelativistic counterpart, first derived by Ferrell and Echenique.[10,11] In both cases, the dependence on impact parameter b is fully contained inside the modified Bessel functions K_m, which behave exponentially at large distances.

Equation (29) explicitly separates the dependence on the dielectric response of the sphere, fully contained in the scattering matrices t_l, from the dependence on the electron trajectory. The latter enters in the coupling constants C_{lm}, which depend exclusively on the electron velocity, and via the impact-parameter dependent Bessel functions just noted. This separation is general as long as the electron moves outside the sphere.

Very interestingly, for relatively small spheres, where only low l's contribute significantly, the dependences on

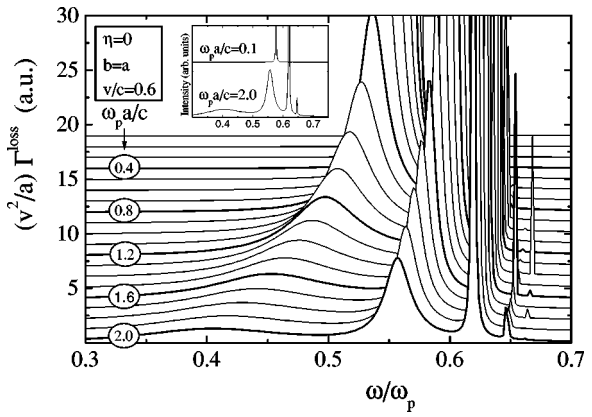

FIG. 4. Energy-loss spectra as a function of energy range ω for electrons passing near a sphere under grazing incidence (i.e., $b=a$; see Fig. 1). The loss probability has been calculated within a fully relativistic approach [Eq. (28)]. The sphere is described by the Drude dielectric function given by Eq. (22) with zero damping. Different sphere radii a have been considered, as shown in the insets, ranging from $a=0.1c/\omega_p$ ($a=13.2$ Å for Al; upper curve) to $a=2c/\omega_p$ ($a=263$ Å for Al; lower curve) in equal steps. The small inset shows the two extreme cases. Consecutive curves are separated by a constant shift of 1 a.u. in order to improve readability.

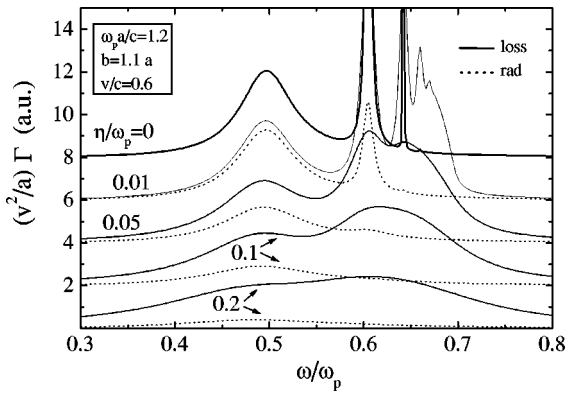

FIG. 5. Energy-loss spectra [$\Gamma=\Gamma^{\rm loss}$, solid curves; Eq. (28)] and photon-emission spectra [$\Gamma=\Gamma^{\rm rad}$, broken curves; Eq. (37)] for an electron moving under the same conditions as in Fig. 4, except that the impact parameter is taken $b=1.1a$ (see Fig. 1), the sphere radius is $a=1.2c/\omega_p$ ($a=157.8$ Å for Al), and the electron gas damping has been varied from $\eta=0$ (upper curve) up to $\eta=0.2\omega_p$ (lower curve), as shown in the insets ($\eta=0.07\omega_p$ for Al). Consecutive curves are separated by a constant shift of 2 a.u. in order to improve readability.

electron velocity and dielectric function are well separated in Eq. (29), so that there are no losses that are enhanced when the Cherenkov condition $(v/c)^2\,{\rm Re}\{\epsilon\}>1$ is fulfilled, and therefore, no Cherenkov effect is expected for the case under consideration, that is, electron trajectories external to the sphere. In the $a\to\infty$ limit, Eq. (29) has to converge to the loss in front of a plane at a fixed distance $b-a$, where Cherenkov terms show up even for external trajectories.[21] In that limit, the contribution of higher-order terms becomes increasingly important, leading to mixing of the dependences on both velocity and dielectric function and resulting in the usual Cherenkov terms.

The coefficients C_{lm} are represented in Fig. 3 as a function of v/c for $l=1-3$. It is clear that the contribution of magnetic modes (broken curves) is much smaller than that of their electric counterpart. Moreover, the dependence of the latter with velocity is relatively smooth for typical STEM energies, though the low- and high-velocity limits show strong variations.

The minor role played by magnetic modes in the coupling coefficients is combined with the smaller magnitude of the magnetic scattering-matrix elements as compared with the electric ones. This is shown in Fig. 2, where ${\rm Im}\{t_l^M\}$ [dotted curves in Figs. 2(a) and 2(b), corresponding to damping $\eta=0$, and solid curves in Figs. 2(e) and 2(f), for damping $\eta=0.07\omega_p$] is systematically smaller than ${\rm Im}\{t_l^E\}$. The smaller the sphere radius, the larger this effect. Actually, t_l^M take significant values only for large spheres (i.e., for $a>c/\omega_p$) in the high-ω region, where the Bessel functions of Eq. (29) dramatically reduce the loss probability.

The loss probability is represented in Figs. 4–8 for different combinations of electron velocity, impact parameter, sphere radius, and dielectric functions. Moreover, the integrated loss probability, defined as

$$\Gamma_{\rm total}^{\rm loss}=\int_0^\infty d\omega\,\Gamma^{\rm loss}(\omega), \tag{32}$$

is studied in Figs. 9 and 10.

E. Dipole approximation and nonrelativistic limit

In the limit of small sphere radius, the scattering-matrix elements scale as $t_l^M\sim(ka)^{2(l+1)}$ and $t_l^E\sim(ka)^{2l+1}$. In particular,

$$t_l^E=\frac{(l+1)(2l+1)}{[(2l+1)!!]^2}\,\frac{\epsilon-1}{l\epsilon+l+1}(ka)^{2l+1},\quad ka\ll 1, \tag{33}$$

and $t_l^M\ll t_l^E$. Therefore, the leading terms in Eq. (29) correspond to electric modes with $l=1$. Keeping only those terms and using the values of A_{lm}^+ and B_{lm} given in the previous section, one finds

$$\Gamma^{\rm loss}(\omega)=\frac{C\omega^2}{v^4\gamma^2}\left[K_1^2\left(\frac{\omega b}{v\gamma}\right)+\frac{1}{\gamma^2}K_0^2\left(\frac{\omega b}{v\gamma}\right)\right],\quad ka\ll 1, \tag{34}$$

where

$$C=\frac{4a^3}{\pi}{\rm Im}\left\{\frac{\epsilon-1}{\epsilon+2}\right\}.$$

Using the Drude dielectric function defined by Eq. (22), taking the $\eta\to 0$ limit, noticing that the plasma frequency is related to the electron gas density n via $\omega_p^2=4\pi n$, and assuming that there is only one electron inside the electron gas that defines the sphere [i.e., $n=3/(4\pi a^3)$], one finds that the total energy loss as defined by Eqs. (25) and (34) is given by the right-hand side of Eq. (34) with $C=2$ and $\omega=\omega_p/\sqrt{3}$

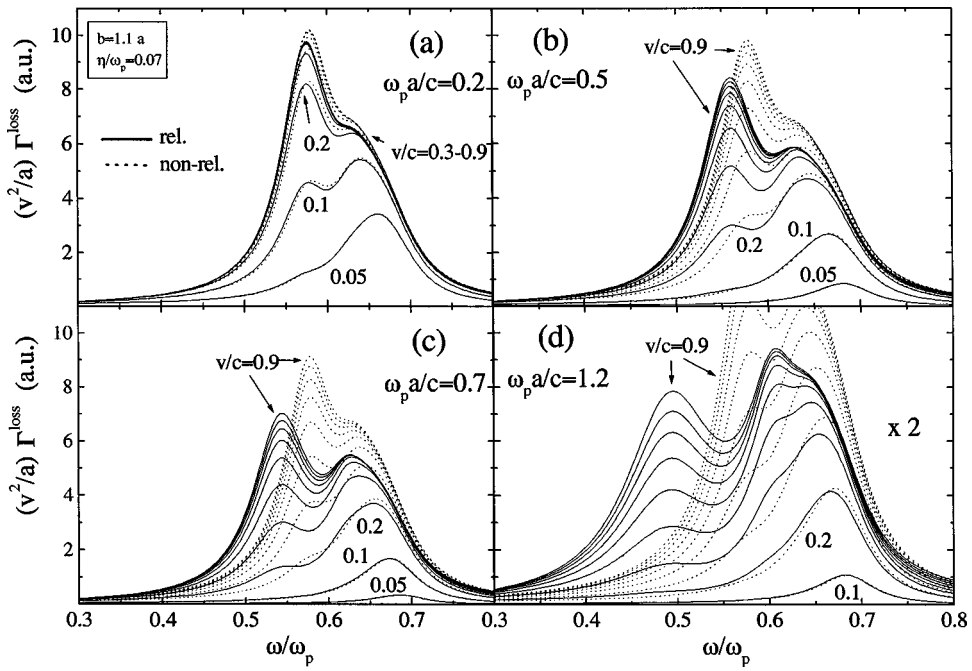

FIG. 6. Comparison between the results obtained from the relativistic theory [solid curves; Eq. (28)] and the nonrelativistic theory [broken curves; Eq. (35)] for electron energy-loss spectra obtained under the same conditions as in Fig. 4 with different combinations of parameters: electron gas damping $\eta=0.07\omega_p$; impact parameter $b=1.1a$; sphere radius $\omega_p a/c=0.2$, 0.5, 0.7, and 1.2 [figures (a), (b), (c), and (d), respectively; $a=26.3$, 65.8, 92.1, and 157.8 Å in the care of Al]. Different electron velocities have been considered in each case as shown in the insets.

(the latter is the dipolar mode of a nonrelativistic sphere). This result coincides with the energy loss suffered by an electron moving near a unit charge subjected to a spring of frequency $\omega_p/\sqrt{3}$.[29] In other words, this demonstrates that the sphere responds like a dipole in the $ka\ll 1$ limit.

Notice that the relativistic effects in Eq. (34) are related to kinematic factors (γ^{-1} factors), leaving the position of the dipole resonance unchanged with respect to the nonrelativistic result (i.e., $\epsilon+2=0$). Therefore, the retardation effects within a small sphere ($ka\ll 1$) do not affect the resonance frequencies.

Equation (29) is thus a generalization of the dipole limit represented by Eq. (34), and the Lorentz contraction of the impact parameter by a factor γ is maintained.

In the nonrelativistic limit, inserting Eq. (A10) into Eq. (15) one obtains $B_{lm}=2ilA^{+}_{lm}$. Then, using Eqs. (29), (30), (31), and (A10), one finds that the contribution to the loss probability originating in magnetic and electric modes scale with c as $c^{2l-1}t^{M}_{l}$ and $c^{2l+1}t^{E}_{l}$, respectively. Then, noticing the scaling of the scattering matrix described at the beginning of this section, one finds that the contribution of magnetic modes vanishes in the nonrelativistic limit, whereas the remaining electric modes contribute as

$$\Gamma^{\rm loss}(\omega)=\frac{4a}{\pi v^2}\sum_{l=1}^{\infty}\sum_{m=-l}^{l}\left(\frac{\omega a}{v}\right)^{2l}\frac{l}{(l+m)!(l-m)!}\times K_m^2\left(\frac{\omega b}{v}\right)\mathrm{Im}\left(\frac{\epsilon-1}{l\epsilon+l+1}\right),\quad ka\ll 1,\quad v/c\ll 1, \tag{35}$$

as found by Ferrell *et al.*[11] Equations (33) and (A10) have been used in the derivation of Eq. (35).

The results derived from Eq. (35) have been compared with the full relativistic calculation of Eq. (29) in Fig. 6.

III. DISCUSSION OF ELECTRON ENERGY LOSS SPECTRA

The natural oscillations of the sphere have a finite width even for real dielectric functions (see Fig. 2). In that case, the loss probability takes nonzero values over extended regions of ω, as Fig. 4 illustrates for different sphere radius (see insets) in the case of grazing trajectories (i.e., $b=a$). The sphere has been described by the Drude dielectric function given by Eq. (22) taking $\eta=0$, and the results have been scaled in order to make the picture valid for any value of ω_p. The figure shows how the position and width of the peaks evolve with the sphere radius in the loss spectra. This is in agreement with the discussion of Fig. 2 above. Incidentally, the surface mode $l=1$ dominates the loss spectra for small sphere radius (see upper curve in the inset), whereas higher-l modes show up as the radius increases. The approximate expressions (23) and (24) for the complex dipole frequency work well up to $\omega_p a/v\approx 1.2$.$-\omega_i$ is directly connected to half width at half maximum of the $l=1$ main feature in the figure (i.e., the peaks of lowest energy).

When a finite damping is considered in the dielectric function, the features of the loss spectra are broadened, and their width is approximately given by the radiative width (i.e., the value for $\eta=0$) plus the damping, as shown in Fig. 5 (solid curves). Notice that the excitation of the different modes results in common broad structures as η increases.

The variation of the loss probability with electron velocity is analyzed in Fig. 6 for different spheres radius. The veloci-

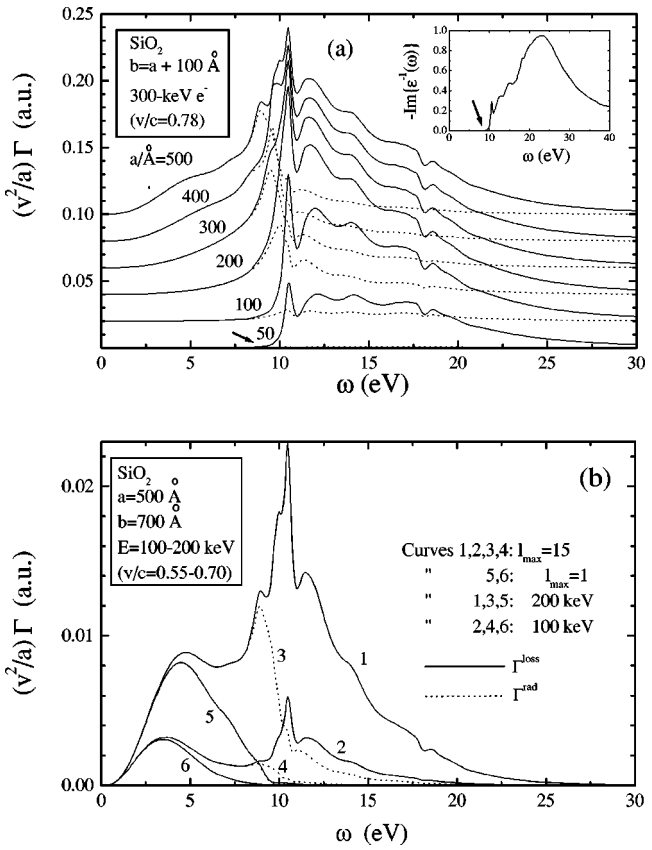

FIG. 7. (a) Comparison between the loss probability ($\Gamma=\Gamma^{\rm loss}$, solid curves) and the radiation emission probability ($\Gamma=\Gamma^{\rm rad}$, broken curves) corresponding to a 300-keV e^- passing at a distance of 100 Å from the surface of a SiO_2 sphere for different values of the sphere radius ranging from $a=50$ Å to $a=500$ Å as shown in the insets. The smaller plot shows the loss function for bulk SiO_2. The small arrows point to the energy below which the dielectric function is real. Consecutive curves are separated by a constant shift of 0.02 a.u. in order to improve readability. (b) Loss probability and photon-emission probability under the same conditions as in (a) for two different electron energies (see insets). The contribution of $l=1$ is given in separate curves (see legend of curve labels), in which case the radiation emission probability cannot be separated from the loss probability.

ties under consideration are shown as labels attached to the different curves. As the velocity of the electron increases, the scaled loss probability $v^2\Gamma^{\rm loss}/a$ becomes larger and the relative role of low-l modes is enhanced in all cases [see the peak at $\omega/\omega_p\approx 0.5$ in Fig. 6(d)]. This result was expected from the velocity dependence of the external electron field, whose range of interaction is $\approx v\gamma/\omega$ according to Eq. (12), so that low-l modes, involving oscillations with a low number of nodes,[33] dominate at large velocities, for which the external potential becomes smoother. The results of the nonrelativistic calculation [Eq. (35)] are represented by broken curves, and they are compared with the full relativistic results [Eq. (29)], shown by solid curves. Both calculations agree relatively well for the smallest sphere radius under consideration, which in the case of aluminum corresponds to $a=26.3$ Å. However, for $a=92.1$ Å [see Fig. 6(c)] the differences are already considerable (both in the position of the features and in their relative magnitude) at electron energies typical of STEM (i.e., $v\sim 0.5c$). The discrepancy for

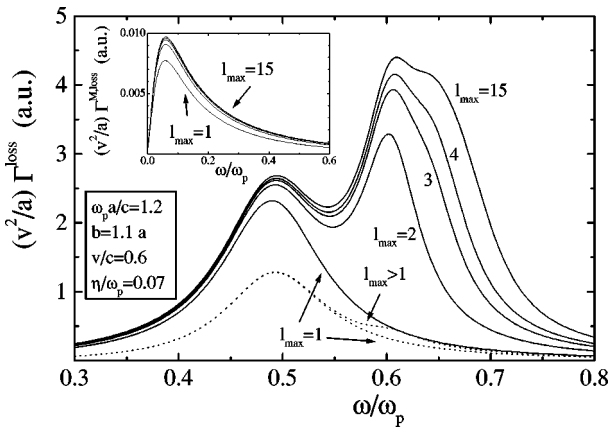

FIG. 8. Contribution to the energy-loss probability ($\Gamma=\Gamma^{\rm loss}$, solid curves) and radiation emission probability ($\Gamma=\Gamma^{\rm rad}$, broken curves) coming from different multipoles for an electron moving near a sphere of radius $a=1.2c/\omega_p$ ($a=157.8$ Å in the case of Al) with impact parameter $b=1.1a$ and velocity $v=0.6c$. The sphere is described by the Drude dielectric function with damping $\eta=0.07\omega_p$. The different curves show the contribution of the first $l_{\rm max}$ values of the orbital momentum number l. The contribution of magnetic modes (M) is shown in the inset. Notice that the probability comes almost entirely from the contribution of electric modes.

$a=157.8$ Å is remarkable [see Fig. 6(d), where the probability has been multiplied by a factor of 2].

Figure 6 confirms that the validity of the nonrelativistic theory is confined to the $\omega_p a/c\ll 1$ and $v/c\ll 1$ limit.

The case of SiO_2 spheres has been considered as well in Fig. 7. This material presents a large band gap that is translated into a region of nearly real dielectric function below 9 eV and above the phonon losses, as shown in the inset of Fig. 7(a). The small arrows indicate the inelastic threshold for creation of electronic excitations in the material. Notice that the loss probability increases with the radius of the sphere in the transparency region. For the largest spheres under consideration and within that frequency region, the energy-loss probability is comparable in magnitude to its value in the absorptive part of the spectrum. The shape of the spectrum above 12 eV changes very little with sphere radius, and the largest variations are produced in the region immediately below the inelastic threshold.

Two different electron velocities have been considered in Fig. 7(b) in order to make clear that the origin of radiation emission under discussion is not connected to the Cherenkov effect: in the case of 100-keV electrons, the Cherenkov condition $(v/c)^2\,{\rm Re}\{\epsilon\}>1$ is not satisfied for $\omega<8.5$ eV, where the dielectric function is nearly real; however, the Cherenkov condition is fulfilled for 200-keV electrons in the whole ω range. Both velocities give rise to qualitatively similar spectra, allowing us to rule out the Cherenkov effect as the origin of radiation for the currently investigated external trajectories. The figure illustrates as well the dominant character of the dipolar mode in the low-ω region.

The contribution of different multipoles to the loss probability is shown in Fig. 8. For the relatively large radius under consideration ($a=157.8$ Å in the case of Al) one needs to sum up to $l\approx 15$, in agreement with previous nonrelativistic results.[10] The inset of the figure shows the contribution of magnetic modes [Eq. (27)] on a different, much

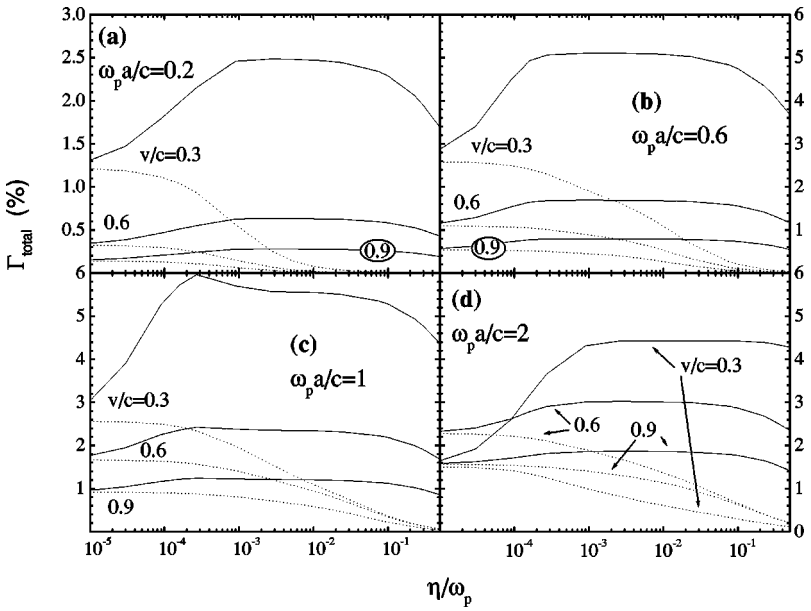

FIG. 9. Dependence of the total loss probability [solid curves; see Eq. (32)] on the damping η for spheres of different radius (see insets) described by a Drude dielectric function. Various electron velocities have been considered in each case as indicated in the labels accompanying the different curves. The total photon-emission probability has also been included for comparison (broken curves). The impact parameter has been taken $b=1.1a$ in all cases.

smaller scale; this permits us to conclude that most of the loss originates in the excitation of electric modes, in good agreement with the results extracted above from Figs. 2 and 3.

The total-loss probability, integrated in energy as shown in Eq. (32), is represented in Figs. 9 and 10 for spheres described by a Drude dielectric function and for SiO_2 spheres, respectively. The dependence of the total-loss probability on the damping η is analyzed in Fig. 9 (solid curves), where different sphere radius have been studied [$\omega_p a/c = 0.2$, 0.6, 1, and 2 in (a), (b), (c), and (d), respectively]. Various velocities have been also considered (see curve labels). The impact parameter has been taken proportional to the sphere radius, $b=1.1a$. The probability shows a smooth dependence on η in all cases. It can take relatively large values even for realistic dampings. Moreover, the probability decreases and becomes featureless as the velocity increases.

Figure 10 shows the dependence of the total-loss probability (solid curves) on impact parameter for different combinations of sphere radius and electron velocities. An overall exponential decay with b is observed, coming from the K_m function of Eq. (29). A decreasing trend with increasing velocity observed in Fig. 9 is observed here for the smallest sphere under consideration ($a=50$ Å in the upper part), and also in the intermediate size sphere ($a=200$ Å) for low values of b/a. However, an increase in the probability with increasing velocity is obtained in the rest of the cases. A more detailed analysis of the probability spectra indicates that this behavior is governed by the radiative losses below the inelastic threshold, which become important for large sphere radius and large b/a ratios.

IV. RADIATION EMISSION INDUCED BY FAST ELECTRONS PASSING NEAR A HOMOGENEOUS SPHERE

The coupling of the electron with radiative modes of the sphere gives rise to radiation emission. The radiated energy can be calculated by integrating the Poynting vector normal to an arbitrarily large sphere centered around the target, that is,

$$\Delta E^{\rm rad}=\frac{c}{4\pi}\int dt \int d\Omega_{\mathbf{r}} r^2 [\mathbf{E}(\mathbf{r},t)\times\mathbf{H}(\mathbf{r},t)]\cdot\hat{\mathbf{r}},$$

where $\mathbf{r}$ points to the surface of the large sphere and the integral over the time has been included. Expressing the fields in terms of their frequency components, one finds

$$\Delta E^{\rm rad}=\int_0^\infty \omega d\omega \int d\Omega_{\mathbf{r}} \Gamma^{\rm rad}(\omega,\Omega_{\mathbf{r}}),$$

where

$$\Gamma^{\rm rad}(\omega,\Omega_{\mathbf{r}})=\frac{r^2}{4\pi^2 k}\,{\rm Re}\{[\mathbf{E}(\omega)\times\mathbf{H}(-\omega)]\cdot\hat{\mathbf{r}}\} \qquad (36)$$

is the probability of emitting a photon of energy ω per unit energy range and unit solid angle around the direction $\Omega_{\mathbf{r}}$. Equation (36) can be computed with the help of the fields calculated in previous sections.

In the $r\to\infty$ limit, only the induced fields contribute to the radiation. In this limit, one can approximate $h_l^{(+)}(kr)\approx i^{-l}e^{ikr}/kr$ in Eqs. (16) and (17), and ∇ can be substituted by $ik\hat{\mathbf{r}}$ in the induced part of the fields given by Eqs. (3) and (5). Substituting the resulting expression into Eq. (36) and integrating over angles, one finds[28]

$$\Gamma^{\rm rad}(\omega)=\int d\Omega_{\mathbf{r}}\Gamma^{\rm rad}(\omega,\Omega_{\mathbf{r}})$$
$$=\frac{1}{4\pi^2 k^3}\sum_{l=1}^{\infty}\sum_{m=-l}^{l} l(l+1)[|\psi_{lm}^{M,{\rm ind}}|^2+|\psi_{lm}^{E,{\rm ind}}|^2].$$

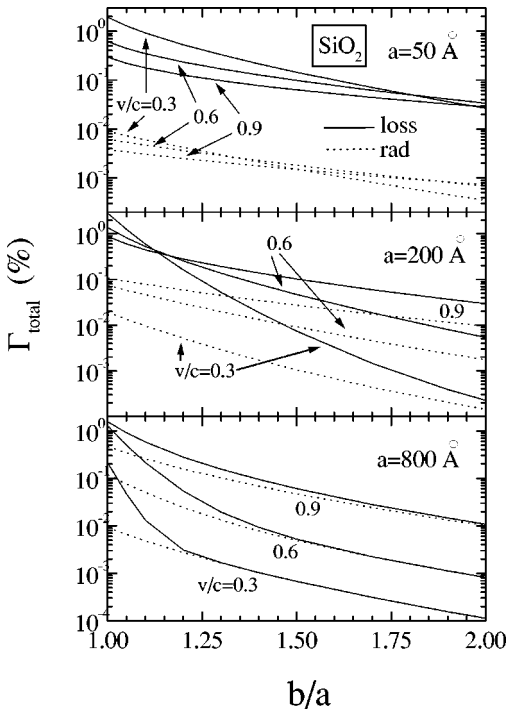

FIG. 10. Dependence of the total loss probability (solid curves) on the ratio b/a (impact parameter to sphere radius) for SiO_2 spheres of different radius (50, 200, and 800 Å, as shown in the insets). Various electron velocities have been considered in each case, as indicated in the labels accompanying the different curves. The total photon-emission probability has also been included for comparison (broken curves).

Finally, using Eqs. (18) and (19), the photon emission probability reduces to

$$\Gamma^{\mathrm{rad}}(\omega)=\frac{1}{c\omega}\sum_{l=1}^{\infty}\sum_{m=-l}^{l}K_m^2\left(\frac{\omega b}{v\gamma}\right)[C_{lm}^M|t_l^M|^2+C_{lm}^E|t_l^E|^2]. \tag{37}$$

For real (either positive or negative) dielectric functions, using basic properties of the spherical Bessel functions in Eqs. (20) and (21), one finds $|t_l^M|^2=\mathrm{Im}\{t_l^M\}$ and $|t_l^E|^2=\mathrm{Im}\{t_l^E\}$. Hence, the radiation emission probability [Eq. (37)] coincides with the loss probability [Eq. (29)] in that case, clearly indicating that the medium is unable to absorb any energy when the absorptive or imaginary part of the dielectric function is zero.

For complex dielectric functions, one has $|t_l^E|^2\leqslant\mathrm{Im}\{t_l^E\}$ and $|t_l^M|^2\leqslant\mathrm{Im}\{t_l^M\}$, as shown in Figs. 2(c)–2(f), where the Drude dielectric function has been used with $\eta=0.07\omega_p$. This result is consistent with the requirement that $\Gamma^{\mathrm{rad}}\leqslant\Gamma^{\mathrm{loss}}$, that is, the energy lost in the form of radiation has to be always smaller than the energy lost by the electron.

Now, Fig. 4, which corresponded to the loss probability for a real Drude dielectric function, can be thought of as showing the photon emission probability.

The effect of electron gas damping η on the radiation-emission probability is shown in Fig. 5 (broken curves). The figure confirms that Γ^{rad} is always smaller than Γ^{loss} and both quantities converge to the same value in the $\eta\to 0$ limit. Moreover, the radiation losses decrease with increasing damping, so that in the competition to absorb energy out of the electron motion the dissipative modes of the sphere dominates for large η. Very interestingly, some of the modes that are present in the loss probability are nearly absent in the photon emission probability (see the features near $\omega\approx 0.65\omega_p$ in the curve corresponding to $\eta=0.01\omega_p$), indicating the different character (either dissipative or radiative) of the different modes.

Below the inelastic threshold (i.e., in the region of real dielectric function) all losses in SiO_2 go into radiation as shown in Fig. 7 (broken curves). This figure illustrates as well how Γ^{rad} increases with increasing sphere radius (i.e., when the relevant condition for the emergence of retardation effects $\omega a/c>1$ is fulfilled).

The decomposition of Γ^{rad} into the contributions coming form different l's is shown in Fig. 8 (broken curves). Notice that the modes $l=1$ and $l=2$ give the dominant contribution to the radiation emission, in contrast to the loss probability, for which higher values of l still contribute significantly. Therefore, the dissipative character is dominant with respect to the radiative one in high-l modes. This can be qualitatively understood using the following argument: the number of nodes of the charge-density perturbation for the different modes increases with l, so that strongly-interacting regions of opposite charge are spatially closer for larger values of l, and hence, retardation effects, including the emergent radiative widths, are weaker. This conclusion is also supported by the widths of the electric modes as observed in the scattering matrix elements (see Fig. 2) in their evolution from $l=1$ to $l=z$.

The total photon-emission probability converges to the total-loss probability in the limit of vanishing damping, as shown in Fig. 9. However, the former (broken curves) decreases with increasing damping, though it can still retain a measurable value ($\approx 0.5\%$ for 100-keV electrons, $b=1.1a$, $a=c/\omega_p$, and damping $\eta=0.07\omega_p$ appropriate for Al). For finite values of the damping, the total photon-emission probability shows a pronounced increase with increasing sphere radius.

In the case of large SiO_2 spheres, the total photon-emission probability converges quickly to the total-loss probability with increasing impact parameter, as shown in the lower part of Fig. 10. This is not true in the case of small spheres (upper part), where retardation effects are not important and the photon-emission probability (broken curves) lies much lower than the loss probability (solid curves).

V. CONCLUSIONS

The Maxwell equations have been analytically solved for an electron moving with constant velocity near a homogeneous sphere. This has permitted us to obtain an analytical expression for the loss probability as a function of the electron impact parameter b. The result [Eq. (29)] looks similar to its nonrelativistic counterpart,[10] and the impact-parameter dependence is subject to a Lorentz contraction via the function $K_m(\omega b/v\gamma)$. The peaks in the loss spectra are shifted with respect to the nonrelativistic case. Moreover, the modes have a natural width that produces a nonzero energy-loss probability spread over a finite range of energies even when the dielectric function of the sphere is real. Explicit approxi-

mate expressions are given for the dipole-complex eigenfrequency in the case of a real Drude dielectric function [see Eqs. (23) and (24)].

It has been shown that most of the energy losses originate in the excitation of electric modes, and magnetic modes are nearly negligible. Furthermore, the bulk of the energy loss comes from low-l modes in spheres of up to several hundred Å in diameter.

Part of the energy loss goes into radiation, due to coupling with radiative modes of the sphere. In particular, when the dielectric function is real, the energy loss and the radiated energy coincide, that is, the medium cannot absorb any energy. This is the case of some materials within certain frequency ranges. As an example, the case of SiO_2, characterized by a large absorption gap, has been studied in detail.

For absorptive media, the presence of a finite imaginary part in the dielectric function increases the loss probability, but reduces the photon-emission probability, since the electromagnetic field originating in the excitation of radiative modes is partly dissipated in the sphere before it escapes in the form of radiation.

Judging from the examples offered in this paper, the probability of emitting radiation induced by the passage of fast electrons is predicted to be large enough to be experimentally detected, leading to the possibility of a microscopy technique based upon the measurement of electron-induced photon-emission spectra.[24]

ACKNOWLEDGMENTS

The author wants to thank A. Howie and P. M. Echenique who, besides suggesting this paper, contributed to it with many critical revisions of the manuscript and helpful and enjoyable discussions. Help and support from the Departamento de Educación del Gobierno Vasco and the Basque Country University are gratefully acknowledged.

APPENDIX A: COUPLING INTEGRALS

This appendix is devoted to derive an analytical solution of the integral

$$M_{lm}^{\pm}(\mathbf{r}_0)=\int dt e^{\pm \mathbf{i}\omega t} h_l^{(+)}(k|\mathbf{r}_0+\mathbf{v}t|) Y_{lm}^*(\Omega_{\mathbf{r}_0+\mathbf{v}t}), \tag{A1}$$

where $h_l^{(+)}(x)$ is the spherical Hankel function,[31] and we assume $\omega>0$.

This integral represents the electromagnetic coupling between a fast electron moving inside a homogeneous medium with constant velocity $\mathbf{v}$ and the multipole component (l,m) of the Green function of the medium, as written in Eqs. (9) and (10). Here, $\mathbf{r}_0$ represents the electron-impact parameter with respect to the origin. The medium is assumed to be described by a frequency-dependent dielectric function $\epsilon_0(\omega)$, so that $k=(\omega/c)\sqrt{\epsilon_0}$ is complex in general, and the square root is taken to yield $\mathrm{Im}\{k\}>0$ (i.e., the electromagnetic field is assumed to vanish at infinity).

The velocity $\mathbf{v}$ will be assumed to be parallel to the z axis. The solution for arbitrarily oriented velocity vectors can be easily obtained from the latter case by using rotation matrices for spherical harmonics.[31] Moreover,

$$M_{lm}^{\pm}(\mathbf{r}_0)=M_{lm}^{\pm}(b,0,0)e^{-\mathbf{i}m\varphi_0}e^{\mp \mathbf{i}\omega z_0/v}, \tag{A2}$$

where (b,φ_0,z_0) are the cylindrical coordinates of $\mathbf{r}_0$, and

$$M_{l,-m}^{\pm}(b,0,0)=(-1)^m M_{l,m}^{\pm}(b,0,0).$$

Therefore, it is enough to consider the case $m\geqslant 0$ and $\varphi_0=z_0=0$.

Our starting point is the time Fourier transform of the retarded Green function[29] [see Eq. (9)]

$$\int dt e^{\pm \mathbf{i}\omega t}\frac{e^{\mathbf{i}k|\mathbf{r}-(b,0,vt)|}}{|\mathbf{r}-(b,0,vt)|}=\frac{2}{v}K_0\left(\frac{\omega}{v\gamma}\sqrt{(x-b)^2+y^2}\right)e^{\pm \mathbf{i}\omega z/v}, \tag{A3}$$

where $\mathbf{r}=(x,y,z)$, $\gamma=1/\sqrt{1-\beta^2}$, and $\beta=kv/\omega$. Again, the square root is taken such that $\mathrm{Re}\{\gamma\}>0$. (Notice that when the electron moves in vacuum, one has $k=\omega/c$, so that $\beta=v/c$ and γ are the standard relativistic-kinematic factors.) Using the expansion of the Green function given in Eq. (10), the left-hand side of Eq. (A3) becomes

$$4\pi k\sum_{l=0}^{\infty}\sum_{m=-l}^{l} j_l(kr)Y_{lm}(\Omega_{\mathbf{r}})M_{lm}^{\pm}(b,0,0)$$

for $r\leqslant b$. Multiplying both this expression and the right-hand side of Eq. (A3) by $Y_{lm}^*(\Omega_{\mathbf{r}})$ and integrating over $\Omega_{\mathbf{r}}=(\theta,\varphi)$, one obtains

$$M_{lm}^{\pm}(b,0,0)=\frac{1}{2\pi kv}\frac{1}{j_l(kr)}\int d\Omega_{\mathbf{r}}Y_{lm}^*(\Omega_{\mathbf{r}}) \times K_0\left(\frac{\omega}{v\gamma}\sqrt{(x-b)^2+y^2}\right)e^{\pm \mathbf{i}\omega z/v}. \tag{A4}$$

The integral over the azimuthal angle can be done by separating the dependence of the spherical harmonic on φ and using the relation[29]

$$\int_{-\pi}^{\pi} d\varphi e^{-\mathrm{i}m\varphi}K_0\left(\frac{\omega}{v\gamma}\sqrt{(x-b)^2+y^2}\right) =2\pi I_m\left(\frac{\omega R}{v\gamma}\right)K_m\left(\frac{\omega b}{v\gamma}\right)\quad (R\leqslant b)$$

where $R=\sqrt{x^2+y^2}$. Then, Eq. (A4) reduces to

$$M_{lm}^{\pm}(b,0,0)=(-1)^m\frac{\alpha_{lm}}{kv}\frac{K_m(\omega b/v\gamma)}{j_l(kr)} \times\int_{-1}^{1} d\mu I_m\left(\frac{\omega R}{v\gamma}\right)e^{\pm \mathbf{i}\omega z/v}P_l^m(\mu), \tag{A5}$$

where $\alpha_{lm}=\sqrt{[(2l+1)/(4\pi)](l-m)!/(l+m)!}$ is the coefficient that accompanies the Legendre function P_l^m to form the spherical harmonic, $R=r\sqrt{1-\mu^2}$, $z=r\mu$, $\mu=\cos\theta$, and the dependence on impact parameter b is fully contained in the modified Bessel functions $K_m(\omega b/v\gamma)$.

The right-hand side of Eq. (A5) must be independent of r. In particular, in the $r\to 0$ limit the spherical Bessel function $j_l(kr)$ goes like $(kr)^l/(2l+1)!!$, leading to an apparent di-

vergence that is compensated by the vanishing integral. Substituting I_m and $\exp(\pm i\omega z/v)$ by their Taylor expansions around $r=0$, one finds

$$(-1)^m\int_{-1}^{1}d\mu I_m\left(\frac{\omega R}{v\gamma}\right)e^{\pm i\omega z/v}P_l^m(\mu)$$
$$=\sum_{j=m}^{\infty}\sum_{s=j}^{\infty}\frac{(\pm i)^{s-j}}{2^j(s-j)![(j-m)/2]![(j+m)/2]!}$$
$$\times\left(\frac{\omega r}{v}\right)^s\frac{1}{\gamma^j}I_{j,s-j}^{lm}, \tag{A6}$$

where the sum over j is restricted to even $j+m$ integral numbers and

$$I_{i_1i_2}^{lm}=(-1)^m\int_{-1}^{1}d\mu(1-\mu^2)^{i_1/2}\mu^{i_2}P_l^m(\mu). \tag{A7}$$

Equation (A7) can be efficiently evaluated using a well-known numerically stable ascending recurrence relation in l for the Legendre functions,[34] leading to

$$(l-m)I_{i_1i_2}^{lm}=(2l-1)I_{i_1,i_2+1}^{l-1,m}-(l+m-1)I_{i_1,i_2}^{l-2,m}$$

for $l>m$. The starting values of this recurrence are $I_{i_1i_2}^{m-1,m}=0$ and

$$I_{i_1i_2}^{mm}=\begin{cases}(-1)^m(2m-1)!!B\left(\dfrac{i_1+m+2}{2},\dfrac{i_2+1}{2}\right), & i_2 \text{ even}\\ 0, & i_2 \text{ odd},\end{cases}$$

where B is the beta function,[35] and $I_{i,i_2}^{m-2,m}=0$.

Upon inspection, one finds that $I_{j,s-j}^{lm}=0$ for $s<l$ and $j\geqslant m$. That is, only the terms $s\geqslant l$ survive in Eq. (A6). Hence, the $r\to 0$ limit of Eq. (A5) finally results in

$$M_{lm}^{\pm}(b,0,0)=\int dte^{\pm i\omega t}h_l^{(+)}[k|(b,0,vt)|]Y_{lm}[\Omega_{(b,0,vt)}]$$
$$=\frac{A_{lm}^{\pm}}{\omega}K_m\left(\frac{\omega b}{v\gamma}\right), \tag{A8}$$

where

$$A_{lm}^{\pm}=\frac{1}{\beta^{l+1}}\sum_{j=m}^{l}\frac{C_j^{lm,\pm}}{\gamma^j}, \tag{A9}$$

$$C_j^{lm,\pm}=\frac{(\pm i)^{l-j}\alpha_{lm}(2l+1)!!}{2^j(l-j)![(j-m)/2]![(j+m)/2]!}I_{j,l-j}^{lm},$$

and the sum is restricted to even $j+m$ integral numbers. The coefficients $A_{lm}^{\pm}$ depend on ω via the dielectric function (see the definition of β and γ above), so that they are independent of ω when the electron moves in vacuum. Of course $A_{lm}^{-}=(A_{lm}^{+})^*$.

In the nonrelativistic limit $k\to 0$, $\beta\to 0$, $\gamma\to 1$, and

$$A_{lm}^{\pm}=\frac{1}{\beta^{l+1}}\frac{(\pm i)^{l+m}(2l+1)!!}{\sqrt{\pi(2l+1)(l-m)!(l+m)!}}. \tag{A10}$$

Then, multiplying Eq. (A8) by $k^{l+1}/(2l-1)!!$ and taking the $k\to 0$ limit, one finds

$$\int dt\frac{e^{\pm i\omega t}}{|(b,0,vt)|^{l+1}}Y_{lm}(\Omega_{(b,0,vt)})$$
$$=\frac{(\pm i)^{l+m}(2l+1)}{\sqrt{\pi(2l+1)(l-m)!(l+m)!}}\frac{\omega^l}{v^{l+1}}K_m\left(\frac{\omega b}{v}\right),$$

which leads to the well-known nonrelativistic result for the electron energy-loss probability in the case of an external trajectory, as found by Ferrell *et al.*[11] (see Sec. II E).

APPENDIX B: THE ELECTRIC SCALAR FUNCTION

The derivation of Eq. (14) is outlined in this appendix.

Inserting Eq. (11) into Eq. (6) and noticing that $(\mathbf{L}\times\nabla)\cdot\nabla=0$, one finds

$$\psi^{E,\mathrm{ext}}(\mathbf{r})=\frac{1}{c}\sum_{l=1}^{\infty}\sum_{m=-l}^{l}\frac{1}{L^2}$$
$$\times[\mathbf{v}\cdot(\mathbf{L}\times\nabla)]j_l(kr)Y_{lm}(\Omega_{\mathbf{r}})\phi_{lm}. \tag{B1}$$

The operator in this expression can be written

$$\mathbf{v}\cdot(\mathbf{L}\times\nabla)=\frac{iv}{2}(L_+\partial_--L_-\partial_+),$$

where $\partial_{\pm}=\partial/\partial x\pm i\partial/\partial y$ and $L_{\pm}=L_x\pm iL_y$. The latter acts only on the angular part of Eq. (B1) (i.e., on the spherical harmonics) according to[29]

$$L_{\pm}Y_{lm}=\sqrt{(l\mp m)(l\pm m+1)}Y_{l,m\pm 1}. \tag{B2}$$

The action of $\partial_{\pm}$ in Eq. (B1) can be studied by realizing that $\partial_{\pm}G_0(\mathbf{r}-\mathbf{r}_t)=-\partial_{\pm}^0G_0(\mathbf{r}-\mathbf{r}_t)$, where $\partial_{\pm}^0$ involves derivatives with respect to $\mathbf{r}_0$ (the dependence on $\mathbf{r}_0$ is contained in ϕ_{lm}) rather than $\mathbf{r}$ [see Eq. (9)]. Now, the relevant identities are [see Eq. (12)]

$$\partial_+^0[K_m(\alpha b)e^{\pm im\varphi_0}]=-\alpha K_{m\pm 1}(\alpha b)e^{\pm i(m\pm 1)\varphi_0} \tag{B3}$$

and

$$\partial_-^0[K_m(\alpha b)e^{\pm im\varphi_0}]=-\alpha K_{m\mp 1}(\alpha b)e^{\pm i(m\mp 1)\varphi_0}, \tag{B4}$$

easily derived by using the recurrence relations of the modified Bessel functions.

Finally, applying Eqs. (B2), (B3), and (B4) to Eqs. (12) and (B1), and making the substitution $L^2\to l(l+1)$, one finds

$$\psi^{E,\mathrm{ext}}(\mathbf{r})=\frac{-2\pi ik}{c\gamma}\sum_{l=1}^{\infty}\sum_{m=-l}^{l}\frac{A_{lm}^{+}}{l(l+1)}j_l(kr)e^{-i\omega z_0/v}$$
$$\times\Bigg[\sqrt{(l-m+1)(l+m)}$$
$$\times K_{m-1}\left(\frac{\omega b}{v\gamma}\right)Y_{l,m-1}(\Omega_{\mathbf{r}})e^{-i(m-1)\varphi_0}$$
$$-\sqrt{(l+m+1)(l-m)}$$
$$\times K_{m+1}\left(\frac{\omega b}{v\gamma}\right)Y_{l,m+1}(\Omega_{\mathbf{r}})e^{-i(m+1)\varphi_0}\Bigg].$$

Now, the summation index m has to be rearranged in order to collect terms that multiply to the same spherical harmonic together. Finally, comparison with Eq. (8) yields Eq. (14).

[1] S. J. Pennycook, D. E. Jesson, and N. D. Browning, Nucl. Instrum. Methods Phys. Res. B **96**, 575 (1995).
[2] L. D. Marks, Solid State Commun. **43**, 727 (1982).
[3] J. M. Cowley, Phys. Rev. B **25**, 1401 (1982).
[4] D. W. McComb and A. Howie, Nucl. Instrum. Methods Phys. Res. B **96**, 569 (1995).
[5] R. D. Averitt, D. Sarkar, and N. J. Halas, Phys. Rev. Lett. **78**, 4217 (1997).
[6] R. H. Ritchie, Phys. Rev. **106**, 874 (1957).
[7] P. M. Echenique and J. B. Pendry, J. Phys. C **8**, 2936 (1975).
[8] N. Zabala, A. Rivacoba, and P. M. Echenique, Surf. Sci. **209**, 465 (1989).
[9] R. García-Molina, A. Gras-Martí, and R. H. Ritchie, Phys. Rev. B **31**, 121 (1985).
[10] T. L. Ferrell and P. M. Echenique, Phys. Rev. Lett. **55**, 1526 (1985).
[11] T. L. Ferrell, R. J. Warmack, V. E. Anderson, and P. M. Echenique, Phys. Rev. B **35**, 7365 (1987).
[12] P. M. Echenique, A. Howie, and D. J. Wheatley, Philos. Mag. B **56**, 335 (1987).
[13] N. Zabala, A. Rivacoba, and P. M. Echenique, Phys. Rev. B **56**, 7623 (1997).
[14] B. L. Illman, V. E. Anderson, R. J. Warmack, and T. L. Ferrell, Phys. Rev. B **38**, 3045 (1988).
[15] A. Rivacoba, N. Zabala, and P. M. Echenique, Phys. Rev. Lett. **69**, 3362 (1992).
[16] A. Rivacoba, J. Aizpurua, and N. Zabala, Scanning Microsc. **9**, 927 (1995).
[17] F. Ouyang and M. Isaacson, Philos. Mag. B **60**, 481 (1989).
[18] F. Ouyang and M. Isaacson, Ultramicroscopy **31**, 345 (1989).
[19] F. J. García de Abajo and J. Aizpurua, Phys. Rev. B **56**, 15 873 (1997).
[20] E. Kröger, Z. Phys. **235**, 403 (1970).
[21] R. García-Molina, A. Gras-Martí, A. Howie, and R. H. Ritchie, J. Phys. C **18**, 5335 (1985).
[22] J. B. Pendry and A. MacKinnon, Phys. Rev. Lett. **69**, 2772 (1992).
[23] J. B. Pendry and L. Martín-Moreno, Phys. Rev. B **50**, 5062 (1994).
[24] F. J. García de Abajo and A. Howie, Phys. Rev. Lett. **80**, 5180 (1998).
[25] R. Fuchs and K. L. Kliewer, J. Opt. Soc. Am. **58**, 319 (1968).
[26] P. M. Echenique, F. J. García de Abajo, V. H. Ponce, and M. E. Uranga, Nucl. Instrum. Methods Phys. Res. B **96**, 583 (1995).
[27] B. Jancovici, Nuovo Cimento **25**, 428 (1962).
[28] F. E. Low, *Classical Field Theory: Electromagnetism and Gravitation* (Wiley, New York, 1997).
[29] J. D. Jackson, *Classical Electrodynamics* (Wiley, New York, 1975).
[30] J. B. Pendry, *Low Energy Electron Diffraction* (Academic Press, London, 1974).
[31] See appendixes of A. Messiah, *Quantum Mechanics* (North-Holland, New York, 1966).
[32] K. Ohtaka and M. Inoue, Phys. Rev. B **25**, 677 (1982).
[33] J. A. Stratton, *Electromagnetic Theory* (McGraw-Hill, New York, 1941).
[34] W. H. Press, S. A. Teukolsky, W. T. Vetterling, and B. P. Flannery, *Numerical Recipes* (Cambridge University Press, New York, 1992).
[35] M. Abramowitz and I. A. Stegun, *Handbook of Mathematical Functions* (Dover Publications, New York, 1972).